

Towards Relaxing the Spherical Solar Radiation Pressure Model for Accurate Orbit Predictions

Michael Lachut*

SERC Limited, Mount Stromlo Observatory, Cotter Road, Weston Creek, Australian Capital Territory, 2611, Australia

James Bennett

SERC Limited, Mount Stromlo Observatory, Cotter Road, Weston Creek, Australian Capital Territory, 2611, Australia

ABSTRACT

The well-known cannonball model has been used ubiquitously to capture the effects of atmospheric drag and solar radiation pressure on satellites and/or space debris for decades. While it lends itself naturally to spherical objects, its validity in the case of non-spherical objects has been debated heavily for years throughout the space situational awareness community. One of the leading motivations to improve orbit predictions by relaxing the spherical assumption, is the ongoing demand for more robust and reliable conjunction assessments.

In this study, we explore the orbit propagation of a flat plate in a near GEO orbit under the influence of solar radiation pressure, using a classical Lambertian BRDF model. Consequently, this approach will account for the spin rate and orientation of the object, which is typically determined in practice using a light curve analysis. Here, simulations will be performed which systematically reduces the spin rate to demonstrate the point at which the spherical model no longer describes the orbital elements of the spinning plate. Further understanding of this threshold would provide insight into when a higher fidelity model should be used, thus resulting in improved orbit propagations. Therefore, the work presented here is of particular interest to organizations and researchers that maintain their own catalog, and/or perform conjunction analyses.

1. INTRODUCTION

Throughout the field of space situational awareness (SSA), the spherical solar radiation pressure (SRP) model is used ubiquitously for orbit determination/propagation (OD/OP) [1–3] of objects in MEO and GEO, where the Earth’s atmosphere has little or no influence on such objects. While this SRP model will yield reliable results from OD/OP for spherical objects [4–7], some argue that it is used in situations where a higher fidelity non-spherical approach should be considered [8]. However, a detailed analysis which provides insight into when either a spherical or non-spherical SRP model should be used – based on the spin rate and orientation – has been relatively overlooked.

For accuracy and reliability it would be fair to argue that all objects should be modeled with high fidelity by considering a non-spherical approach. This would potentially result in benefits, such as: i. enhancing accuracy and reduce uncertainties in propagations, particularly for high-area-to-mass ratio (HAMR) objects [9], ii. improve catalog maintenance [8], and iii. lead to more accurate and reliable conjunction assessments. Though, taking all objects to be non-spherical could also lead to disadvantages, like: i. hinder computational performance when performing an all-on-all conjunction assessment, ii. lead to higher uncertainties if a poor/inaccurate non-spherical model is used, and iii. make a catalog more complex than necessary, especially in cases where the spherical SRP model yields sufficient results. In addition, methods used to characterize objects using non-spherical approaches are usually quite sophisticated and complex [10], thus may put huge strains on systems if used for a large number of objects; there is also an increase in observational data requirements to parametrize the models. The ability to be able to make informed decisions on when spherical or non-spherical models could or should be used, would benefit the SSA community. Particularly those researchers and institutes which maintain their own catalog and/or perform conjunction analyses.

In practice, orbit propagations are typically used for conjunction assessments, catalog maintenance, and perhaps understanding the evolution of a debris fields over long periods. The prediction spans and accuracy requirements vary depending on the application. For a conjunction assessment, one would typically propagate from the current state epoch to only about 10 days [11] in order to maintain higher accuracy. The acceptable level of uncertainty in this case

*Email: michaellachut@serc.org.au

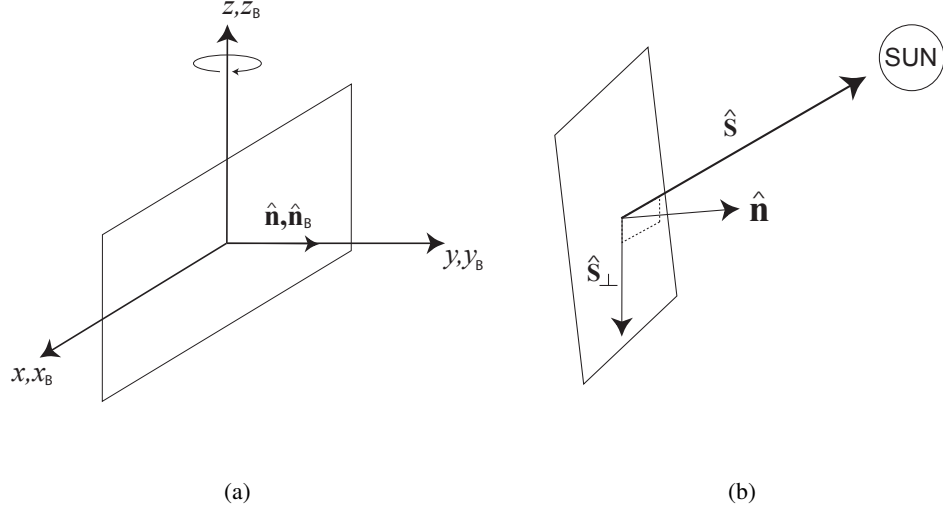


Fig. 1. (a) Schematic of the flat plate illustrating that the normal in the body-fixed frame \hat{n}_B points in the positive y_B -direction and rotates about the z_B -axis. This diagram corresponds to the initial orientation $(0^\circ, 0^\circ, 0^\circ)$, where the body-fixed coordinate system coincides with the inertial coordinate system. (b) Schematic of the flat plate showing the unit vector pointing to the sun \hat{s} , the unit vector perpendicular to the sun vector \hat{s}_\perp , and the plates normal vector \hat{n} in the inertial reference system.

is bounded by the so-called safety zone which is the range between two objects in close proximity [1]. This safety threshold is usually specified by a satellite owner operator or organizations that perform conjunctions analysis, like SOCRATES who set theirs at 5km and propagate out to 7 days [1, 11]. At the Space Environment Research Centre (SERC)¹, we aim to set our safety zone to 1km to suit the requirements of our partners at OPTUS². Furthermore, in the case of catalog maintenance, propagations could span from weeks to months with reacquisition success depending on the sensor's field of view, assuming the object is detectable. Enhancing the accuracy of orbit predictions for catalog maintenance would allow for longer orbit prediction spans and a reduction in the amount of tracking for a given object. This would improve the efficiency of sensors by allowing them to be free to track other objects. In contrast, when interested in the long term evolution of debris fields over month to years (or even centuries), knowing the exact position of a single object at a specific time is not so important. Instead, this type of analysis would investigate the behavior of the osculating elements over long periods [12, 13].

In this analysis, we will focus on a spinning flat plate in a near-GEO orbit. Since one of the metrics of a conjunction analysis is the safety zone (or proximity threshold), the aim here is to examine when the (Euclidean) separation between the position predicted by the spherical SRP model and a higher fidelity approach – which takes into account the orientation and spin rate of the plate – exceeds that threshold. So to abide by the requested safety zone of 1km for OPTUS, this investigation will explore when the separation goes beyond that threshold during a 10 day propagation span. Simulations will be performed where the spin rate of the plate is systematically reduced to demonstrate changes in the separation; this will be repeated for various orientations. Modification to the semi-major axis as the spin rate is reduced will also be investigated to provide insight into when the effects of coupling between the orbital and spin periods are significant. It will be shown that when this coupling is weak, the separation is highly dependent on the orientation. In contrast, as the effects of coupling becomes more pronounced we will show that the separation grows rapidly, regardless of the orientation.

2. METHOD

In this section, the methodology is derived that will be used throughout this study. First we define the orientation of the plate and how to calculate the effective area exposed to the sun. The SRP accelerations that will be used are then presented followed by an outline of the assumptions and techniques used throughout this analysis.

¹Cooperative Research Centre for Space Environment Management (SERC Limited) – further details available at <http://www.serc.org.au/>. Date last accessed 9-14-16.

²OPTUS Satellite – further information available at <http://www.optus.com.au/business/broadband-internet/networking-solutions/satellite/about>. Date last accessed 9-14-16.

2.1. Plate Orientation and Effective Area

We begin by defining the orientation of the plate in the satellite body-fixed frame. The plate is assumed to be flat with its normal $\hat{\mathbf{n}}_B$ pointing in the y_B -direction and rotates about the z_B -axis of that coordinate system; see Fig. 1(a). The effective area A_\odot facing the sun is therefore defined as,

$$A_\odot = A_{\text{plate}} |\hat{\mathbf{n}} \cdot \hat{\mathbf{s}}|, \quad (1)$$

where A_{plate} is the total area of the plate, $\hat{\mathbf{s}}$ is the vector pointing towards the sun and $\hat{\mathbf{n}}$ is the normal to the plate in the inertial coordinate frame [refer to Fig. 1(b)] which is given by,

$$\hat{\mathbf{n}} = \text{ROT}_1(\theta_x) \cdot \text{ROT}_2(\theta_y) \cdot \text{ROT}_3(\theta_z) \cdot \text{ROT}_3(\omega_{\text{spin}} t) \cdot \hat{\mathbf{n}}_B, \quad (2)$$

where ROT_1 , ROT_2 , ROT_3 are transformation matrices corresponding to rotations about the x, y, z -axis in the inertial coordinate frame, respectively, $\theta_x, \theta_y, \theta_z$, are the rotation angles, ω_{spin} is the spinning plate's angular frequency, and t is time. It is important to emphasize that the first three rotation matrices in Eq. (2) only define the initial orientations and do not change as a function of time; the last transformation matrix of that equation defines the rotation of the plate about the z_B -axis of the body-fixed frame; see Fig. 1(a). Note that initial rotations specified throughout this analysis will henceforth take the following form: $(\theta_x, \theta_y, \theta_z)$.

2.2. Solar Radiation Pressure Models and Equivalent γ_{eqv}

This investigation will consider two SRP accelerations, one based on the spherical assumption,

$$\mathbf{a}_{\text{SRP}}^{(S)} = -\nu \frac{p_{\text{SR}} C_R^{(s)} A_{\text{sph}}}{m} \hat{\mathbf{s}}, \quad (3)$$

where ν , p_{SR} , $C_R^{(s)}$, A_{sph} and m are the shadow factor, solar pressure coefficient, coefficient of reflectivity, spherical cross-sectional area, and mass, respectively. While the other SRP acceleration, which is applicable to a spinning plate, is based on a Lambertian BRDF model [1, 8],

$$\mathbf{a}_{\text{SRP}}^{(L)} = -\nu \frac{p_{\text{SR}} A_\odot}{m} \left[2 (C_d/3 + C_s |\hat{\mathbf{n}} \cdot \hat{\mathbf{s}}|) \hat{\mathbf{n}} + (1 - C_s) \hat{\mathbf{s}} \right], \quad (4)$$

where C_d and C_s are the diffuse and specular coefficients of reflectivity, respectively. Notwithstanding other more general Non-Lambertian BRDF models [8, 13], which may also account for thermal emissivity [9, 14], they go beyond the scope of this analysis.

Since our aim is to measure the separation between the position resulting from using both accelerations defined above, we require a method to estimate the (equivalent) so called $\gamma_{\text{eqv}} = C_R^{(s)} A_{\text{sph}}/m$ which will be used for propagations using the spherical SRP model; Eq. (3). However, since the normal vector, $\hat{\mathbf{n}}$, in general contains a component in the perpendicular direction to the sun, $\hat{\mathbf{s}}_\perp$ [15] [see Fig. 1(b)], we substitute $\hat{\mathbf{n}} = |\hat{\mathbf{n}} \cdot \hat{\mathbf{s}}| \hat{\mathbf{s}} + \sqrt{1 - |\hat{\mathbf{n}} \cdot \hat{\mathbf{s}}|^2} \hat{\mathbf{s}}_\perp$ into Eq. (4) to yield,

$$\begin{aligned} \mathbf{a}_{\text{SRP}}^{(L)} = & -\nu \frac{p_{\text{SR}} A_\odot}{m} \left\{ \left[2 (C_d/3 + C_s |\hat{\mathbf{n}} \cdot \hat{\mathbf{s}}|) |\hat{\mathbf{n}} \cdot \hat{\mathbf{s}}| + (1 - C_s) \right] \hat{\mathbf{s}} \right. \\ & \left. + 2 (C_d/3 + C_s |\hat{\mathbf{n}} \cdot \hat{\mathbf{s}}|) \sqrt{1 - |\hat{\mathbf{n}} \cdot \hat{\mathbf{s}}|^2} \hat{\mathbf{s}}_\perp \right\}. \end{aligned} \quad (5)$$

Now since the spherical SRP model [Eq. (3)] is oblivious to components perpendicular to the sun, the second term within the curly parenthesis is ignored and an average of the first term is taken to give,

$$\gamma_{\text{eqv}} = \frac{C_R^{(s)} A_{\text{sph}}}{m} \equiv \frac{A_{\text{plate}}}{m} \frac{1}{T_{\text{spin}}} \int_0^{T_{\text{spin}}} |\hat{\mathbf{n}} \cdot \hat{\mathbf{s}}| \left[2 \left(\frac{C_d}{3} + C_s |\hat{\mathbf{n}} \cdot \hat{\mathbf{s}}| \right) |\hat{\mathbf{n}} \cdot \hat{\mathbf{s}}| + (1 - C_s) \right] dt. \quad (6)$$

Similar techniques of averaging used to derive Eq. (6) have been used in other analytical studies [13].

2.3. Outline of Assumptions

To proceed, Eq. (6) will be used to estimate γ_{eqv} for simulations involving the spherical SRP acceleration, whereas, $C_d = C_s = 0.313$ is used when propagating the spinning plate; these are typical values for MLI materials [12]. In an attempt to model a plate in a realistic near-GEO orbit, we define our initial state as the two-line element (TLE) of the MSG-2 cooler cover near epoch 0:00:00 UTC of the vernal equinox of 2016 (3-20-2016). The maximum area-to-mass of the plate, $A_{plate}/m = 0.23$ [10], is also adopted from the MSG-2 cooler cover; note the mass remains fixed in all cases. Other perturbing forces will consist of a 10th order, 10th degree EGM-96 non-spherical earth gravity model and third-body Luna gravity. The center of mass always coincides with the geometric center, i.e., no torques are considered. To perform all propagations, the General Mission Analysis Tool (GMAT)³ will be used with predictions spans of 10 days. The EME2000 inertial coordinate frame is used throughout.

3. RESULTS AND DISCUSSION

In this section, we first calculate the equivalent γ_{eqv} needed for propagations based on the spherical SRP model. The separation in the position from the spherical and spinning plate predictions are presented for the shortest spin period considered in this analysis. Results for the semi-major axis and separations are then demonstrated as the spin rate is systematically reduced.

3.1. Calculating the Equivalent γ_{eqv}

To begin, Eq. (6) is used to calculate the ratio between the cross-sectional areas of the sphere and plate A_{sph}/A_{plate} , when $C_d = C_s = 0$; by convention the equivalent area of the sphere is fixed and accounts for non-zero diffuse and specular reflectivity by adjusting the coefficient of reflectivity, $C_R^{(s)}$. The (equivalent) coefficient of reflectivity of the sphere $C_R^{(s)}$, when $C_d = C_s = 0.313$, is then calculated using the same equation [Eq. (6)]; results provided in Tab. 1. Substituting the calculated A_{sph}/A_{plate} , $C_R^{(s)}$ and $A_{plate}/m = 0.23$ into the middle term of Eq. (6) yields the equivalent γ_{eqv} , which is given in Tab. 1 for all orientations considered. These values for γ_{eqv} are then used in propagations where the spherical SRP model is used.

Tab. 1. Ratio between the sphere and plate cross-sectional areas A_{sph}/A_{plate} when $C_d = C_s = 0$, coefficient of reflectivity of the sphere $C_R^{(s)}$ and equivalent γ_{eqv} when $C_d = C_s = 0.313$.

Initial Orientation	$A_{sph}/A_{plate} (C_d = C_s = 0)$	$C_R^{(s)} (C_d = C_s = 0.313)$	$\gamma_{eqv} (C_d = C_s = 0.313)$
$(0^\circ, 0^\circ, 0^\circ), (45^\circ, 0^\circ, 0^\circ)$	0.63662	1.26822	0.185696
$(90^\circ, 0^\circ, 0^\circ), (0^\circ, 0^\circ, 45^\circ)$			
$(0^\circ, 0^\circ, 90^\circ)$	0.450158	1.01155	0.104732
$(0^\circ, 45^\circ, 0^\circ)$			

3.2. Projected Separation in the Position

Next, we investigate the separation in the position predicted by simulations using the spherical SRP model with that of the spinning plate, when $T_{spin} = 20$ sec, which is the shortest considered here. Fig. 2(a) presents the separation, $\Delta \mathbf{r} = \mathbf{r}_{plate} - \mathbf{r}_{sph}$, projected onto the radial, along-track and cross-track directions of the RSW coordinate system [1], for orientation $(0^\circ, 0^\circ, 0^\circ)$. In Fig. 2(a), it is shown that the separation in all directions is periodic with an angular frequency consistent with that of the orbital frequency, and an amplitude which grows with time. Fig. 2(a) illustrates a noticeable separation after approximately two orbital periods with the dominate growth occurring in the along-track direction (red curve); the least increase in $\Delta \mathbf{r}$ appears in the cross-track direction (green curve). Interestingly, when the separation in the along-track direction is at a local maximum/minimum the radial separation (blue curve) will be zero, and vice versa. So what this means physically is that any difference between the spherical and spinning plate SRP accelerations changes from pointing in the radial and along-track direction throughout the orbit, as expected. Additionally, Fig. 2(a) shows a secular drift in both the along-track and cross-track directions, but not in the radial direction. Importantly, we see that the magnitude of the maximum separation in the along-track direction is only about 40m, which is small for an object in a near-GEO orbit. This demonstrates that simulations for the object of interest using the spherical SRP model yields a reasonable prediction when compared to using the higher fidelity

³Release version R2015a available at <http://gmatcentral.org/>. Date last accessed 9-14-16

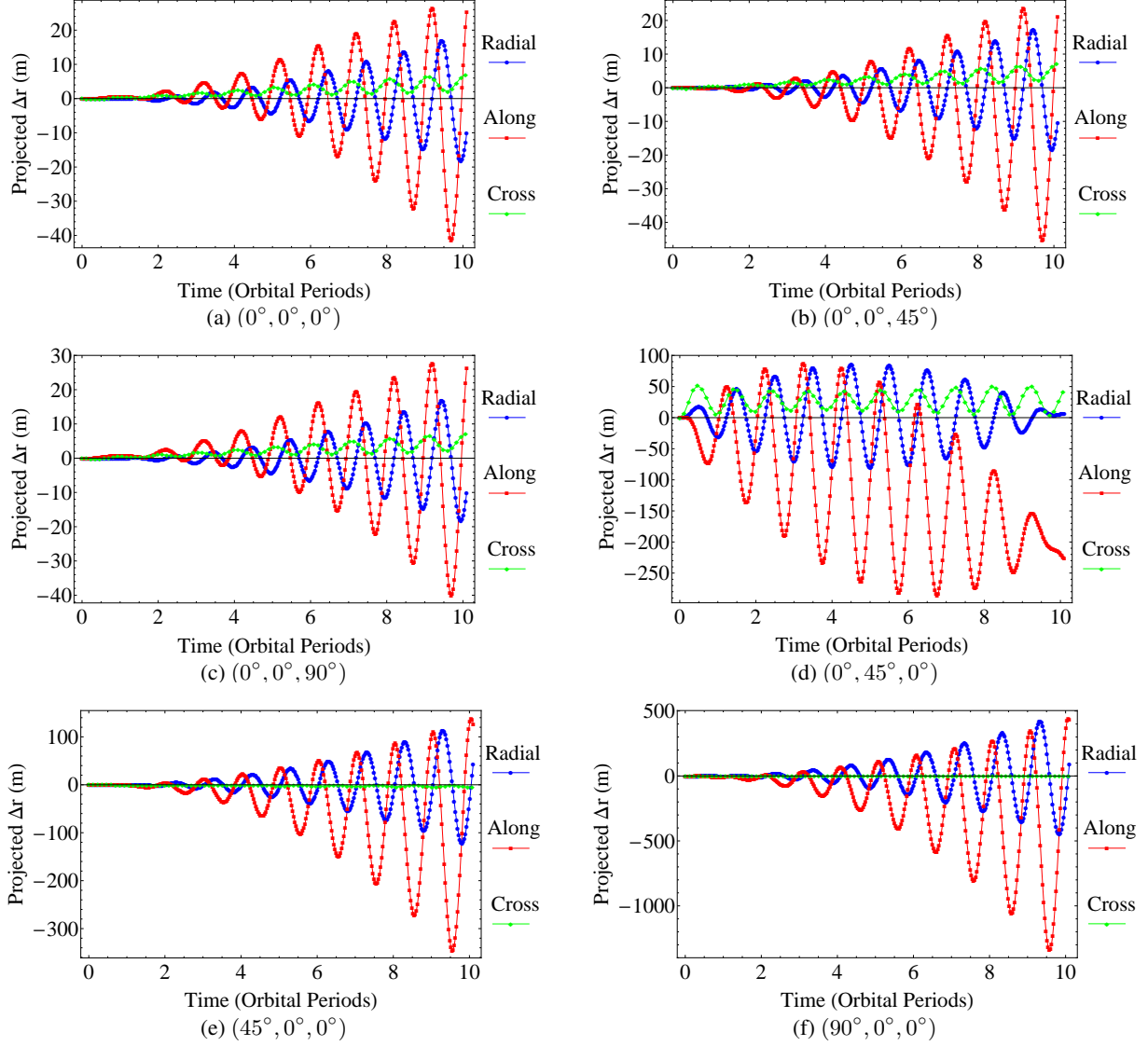


Fig. 2. Projections in the Radial (Blue), Along-track (Red) and Cross-track (Green) direction of the separation, $\Delta \mathbf{r} = \mathbf{r}_{\text{plate}} - \mathbf{r}_{\text{sph}}$, between the position predicted by simulations using the spherical SRP model with respect to that using the BRDF model applied to a spinning plate where $T_{\text{spin}} = 20$ sec. The orientations are indicated in the sub-captions of each sub-figure.

approach, which takes $T_{\text{spin}} = 20$ seconds and the orientation as $(0^\circ, 0^\circ, 0^\circ)$ into account. Moreover, rotating the initial orientation about the z -axis by 45° and 90° yields virtually identical results, cf. Figs. 2(a)–2(c).

When setting the initial orientation to $(0^\circ, 45^\circ, 0^\circ)$, we notice considerably different behavior in the separation compared to Figs. 2(a)–2(c). The results for this orientation are presented in Fig. 2(d), where almost immediately after $t = 0$ there is a growth in the separation. Perhaps most notably in Fig. 2(d) are the beats that appear in the radial and along-track directions, with a strong secular drift only occurring in the latter direction. Fig. 2(d) shows that the maximum separation is in the along-track direction, but with a maximum magnitude now approaching 300m. This value is almost an order of magnitude larger than that by rotating about the z -axis, but is still within the 1km threshold. Furthermore, rotating about the x -axis exhibited similar behavior to the case which rotated about the z -axis, with the following exceptions as the rotation angle, θ_x , increases: i. the maximum separation in the radial and along-track directions grows; and, ii. the secular drift becomes slightly stronger in the along-track direction; cf. Figs. 2(a)–2(c), 2(e) and 2(f). Significantly, Fig. 2(f) demonstrates that the along-track separation goes beyond the 1km threshold after about 9 orbital periods. This suggests that for the object of interest here, we may need to use a higher fidelity approach

for this particular orientation, i.e., $(90^\circ, 0^\circ, 0^\circ)$, even for a fast spinning object.

This increase in the maximum separation as the initial rotation about the x -axis increases can be explained by considering, for example, the case of an initial rotation $(90^\circ, 0^\circ, 0^\circ)$. Since the initial epoch is the vernal equinox, the plate's normal, \hat{n} , is parallel to the sun vector, \hat{s} , when the area is fully exposed; see Fig. 3. Consequently, any component of the force resulting from specular and diffuse reflections in the perpendicular to the sun direction, \hat{s}_\perp , will be averaged out if the plate spins at a sufficient rate. Then as the sun moves position over the given prediction span, the normal, \hat{n} , will no longer be parallel to the sun vector, \hat{s} , at maximum exposure. This now yields a resultant force with a component which remains unchanged as the plate spins but grows in magnitude as the sun moves position. The direction of this component is such that it is both in the direction of \hat{s}_\perp and lies in the plane defined by \hat{s} (or \hat{s}_\perp), and a vector parallel to the rotation axis z_B . As such, this component of the resultant force can not be averaged out in spite of the plate's spin rate or captured by the spherical SRP model. Therefore, it is not surprising that a larger separation occurs over the 10 day prediction span when there is an initial rotation about the x -axis.

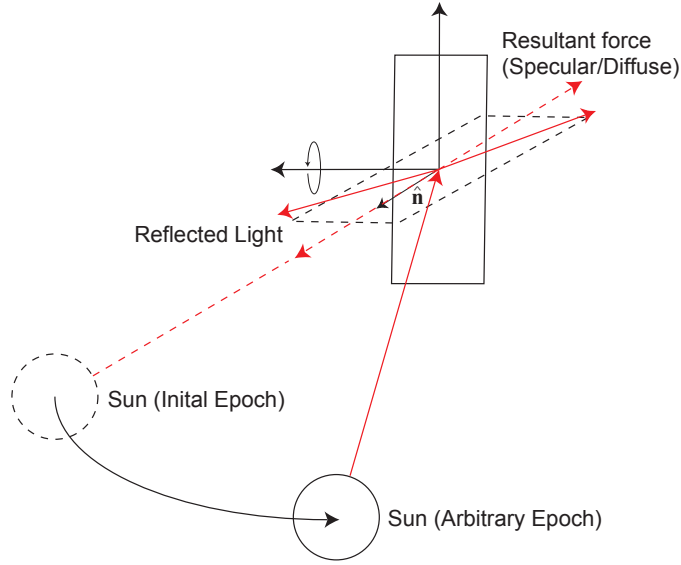


Fig. 3. Schematic showing the change in the position of the sun throughout the 10 day prediction span for orientation $(90^\circ, 0^\circ, 0^\circ)$.

3.3. Analyzing the Change in the Semi-Major Axis

In Sec. 3.2, we only considered one spin period which was the shortest used in this analysis. We will now analyze the case when the spin period is systematically increased. To begin, let us first consider investigating the variation in the semi-major axis (SMA) of the spinning plate, a_{Plate} . This is because accelerations in the radial and along-track directions have a direct impact on a_{Plate} in accordance with Gaussian variation of parameter equations (VOP) [1]; it also allows us to clearly observe when the coupling between the orbital and spin period takes effect.

For $T_{\text{spin}} = 200$ and an initial orientation $(0^\circ, 0^\circ, 0^\circ)$, Fig. 4(a) presents the difference in the SMA for the higher fidelity spinning plate SRP model to that in the absence of SRP, $a_{\text{Plate}} - a_{\text{NoSRP}}$, i.e., when only third body Luna gravity and non-spherical Earth gravity is considered. The corresponding fit to the curve in Fig. 4(a) is given by,

$$a_{\text{Plate}} - a_{\text{NoSRP}} = 162.7 + 314 \cos(6.4t + 1.3\pi), \quad (7)$$

in meters, where the angular frequency of $\omega_{\text{orbit}} = 6.4 \text{ rad/day}$ is consistent with the large peak clearly visible in the results of the FFT analysis provided in Fig. 4(b). Importantly, the results in the case of the spherical SRP model (red curve) are virtually identical to that provided in Figs. 4(a) and 4(b) of the spinning plate. This demonstrates that the coupling between the orbital and spin frequency is negligible when the plate spins at a sufficient rate. In addition, the behavior observed in Figs. 4(a) and 4(b) is expected for a sphere (or quickly spinning object) since SRP adds energy to the system when the object moves away from the sun, and removes energy when moving towards the sun throughout its orbit. It is also important to note that while there is no clear secular drift in $a_{\text{Plate}} - a_{\text{NoSRP}}$ over time in Fig. 4(a), objects transitioning through the earth shadow for longer periods may exhibit stronger secular drifts due to the imbalanced distribution of solar radiation; refer to Fig. 3 of [15].

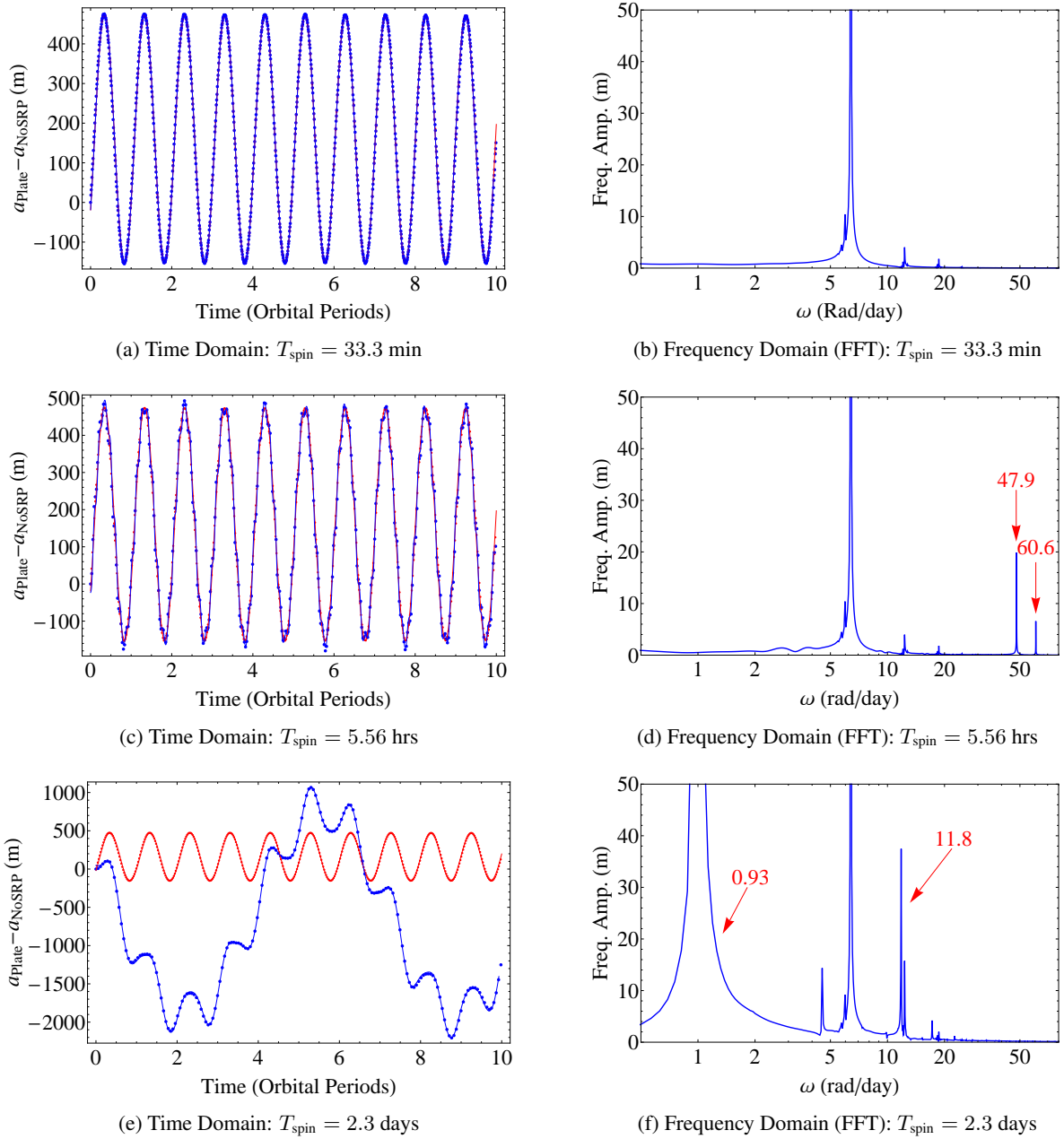


Fig. 4. (a),(c),(e) (Blue) Difference between the SMA of the spinning plate and SMA in the absence of SRP where only Luna gravity and non-spherical earth gravity considered, $a_{\text{plate}} - a_{\text{NoSRP}}$, for various spin periods indicated in figures; (Red) Difference between the SMA of the spherical model and SMA in the absence of SRP, $a_{\text{sphere}} - a_{\text{NoSRP}}$. (b),(d),(f) Frequency domain results for $a_{\text{plate}} - a_{\text{NoSRP}}$ using a Fast Fourier Transform (FFT) analysis for various spin periods indicated in figures. Results correspond to $(0^\circ, 0^\circ, 0^\circ)$ orientation.

Observing Fig. 4(c), we see that in the case when $T_{\text{spin}} = 5.56$ hours the difference in the SMA, $a_{\text{plate}} - a_{\text{NoSRP}}$, still resembles the characteristic behavior resulting from using the spherical SRP model (red curve). Although, now there is an additional effect which is slightly modifying the overall behavior of $a_{\text{plate}} - a_{\text{NoSRP}}$. The results of the FFT analysis presented in Fig. 4(d), show that two additional peaks have appeared on the right-hand-side. Since the spin period is now approaching a quarter of the orbital period, the additional behavior observed in Figs. 4(c) and 4(d) may be attributed to coupling between the orbital and spin frequency. In order to verify this assumption, we propose the

expansion for the difference in the SMA as follows:

$$a_{\text{Plate}} - a_{\text{NoSRP}} = D + \sum_{n=-N}^N B_n \cos[(\omega_{\text{orbit}} - n\omega_{\text{spin}})t + \beta\pi], \quad (8)$$

where ω_{orbit} , ω_{spin} , n , N , β , B_n and D are the orbital angular frequency, angular spin frequency, frequency number, half the total number of terms in addition to the spherical case when $n = 0$, phase angle, amplitudes, and DC offset, respectively. In Eq. (8), the coupling is represented by calculating the frequencies of each term in the expansion using a linear combination of the orbital frequency, and a positive/negative multiple of the spin frequency. Now using Eq. (8) to fit the data of Fig. 4(c) yields,

$$a_{\text{Plate}} - a_{\text{NoSRP}} = 163.8 + 315.3 \cos(6.4t + 1.3\pi) + 26.1 \cos(47.9t + 1.3\pi) - 8.2 \cos(60.6t + 1.3\pi). \quad (9)$$

Notice that Eq. (9) still contains the solution for the spherical case, when $n = 0$, but is now superimposed by two extra terms. Importantly, the angular frequency in those second and third terms of Eq. (9) is consistent with the extra peaks observed in the results of the FFT analysis presented in Fig. 4(d).

Now considering the case when $T_{\text{spin}} = 2.3$ days, the results provided in Fig. 4(e) shows a large difference in $a_{\text{Plate}} - a_{\text{NoSRP}}$ (blue curve), compared to $a_{\text{Sphere}} - a_{\text{NoSRP}}$ (red curve). Once again, if Eq. (8) is used to fit the data of Fig. 4(e), we obtain,

$$a_{\text{Plate}} - a_{\text{NoSRP}} = -394.8 + 293 \cos(6.4t + 1.3\pi) + 1.4 \times 10^3 \cos(0.93t + 0.4\pi) - 43.2 \cos(11.8t + 1.3\pi), \quad (10)$$

where only the two dominant terms in addition to the case resembling the spherical solution are provided. In this case, when $T_{\text{spin}} = 2.3$ days, we see a slight decrease in the amplitude of the component corresponding to the spherical solution, but a dramatic reduction in the DC offset of over 500 m. However, both this amplitude and difference in the DC offset are dwarfed by the amplitude of the second term of Eq. (10). Taking note of the angular frequencies once more in the second and third terms of Eq. (10), reveals again that they are consistent with the peaks of the FFT analysis given in Fig. 4(f). These results presented in Figs. 4(c)–4(f), and the discussion above, therefore demonstrate that the coupling between the orbital and spin frequency are driving the distinctive behavior we see in the difference in the SMA of the plate, $a_{\text{Plate}} - a_{\text{NoSRP}}$, when $T_{\text{spin}} \gtrsim 6$ hours. It is important to note that repeating this analysis for other orientations results in a similar conclusion.

Next, we build on the above analysis by considering the amplitudes for the spherical component and the two dominant contributions as functions of the spin period T_{spin} , where Fig. 5(a) demonstrates this for the initial orientation $(0^\circ, 0^\circ, 0^\circ)$. In Fig. 5(a), the amplitude for the spherical case (green curve) remains unchanged as T_{spin} varies, indicating that the spherical component is always present regardless of the spin rate. Similarly, in that figure we see the DC offset (purple curve) remain constant except when T_{spin} approaches ≈ 6 hrs. Fig. 5(a) also shows that the amplitude for the next most dominate contribution (blue curve), corresponding to $n = -2$ in Eq. (8), is $< 1\%$ of the spherical component's amplitude when $T_{\text{spin}} \lesssim 30$ minutes. Now as T_{spin} increases the amplitude corresponding to $n = -2$ increases linearly since the slope of the Log-Log plot is approximately 1 up until $T_{\text{spin}} \approx 6$ hours (or $1/4T_{\text{orbit}}$). Interestingly, for $T_{\text{spin}} \gtrsim 6$ hours the slope grows with increasing T_{spin} , which is consistent to when the coupling began to have a significant effect on the difference in the SMA in the above discussion regarding the results of Fig. 4. Moreover, the second most dominant term corresponding to when $n = 2$ (red curve) is lower in magnitude but behaves similar to the case where $n = -2$ until $T_{\text{spin}} \approx 6$ hours, after at which the slope decreases for increasing T_{spin} .

Now setting the initial rotation about the z -axis to 45° and then 90° , yields virtually no change in the magnitude and behavior of the amplitudes, with the exception of the DC offset which varies when $T_{\text{spin}} \gtrsim 6$ hours; cf. Figs. 5(a)–5(c). Furthermore, looking at the results for rotating about the y -axis by 45° in Fig. 5(d), reveals that only the magnitudes of the amplitudes in all cases decreases uniformly in comparison to the cases represented in Figs. 5(a)–5(c). This is expected for this particular initial orientation $(0^\circ, 45^\circ, 0^\circ)$ since the maximum effective area, A_\odot , never reaches the total area of the plate; unlike all other orientations. Observing the results of Figs. 5(e) and 5(f), we notice that rotating about the x -axis still preserves the characteristic behavior demonstrated in Figs. 5(a)–5(d). However, the separation between the amplitudes for the dominant terms other than the spherical component is reduced as θ_x increases from 0° to 90° ; cf. Figs. 5(a), 5(e) and 5(f). Finally, the results presented in Fig. 5 shows qualitatively that the behavior of the changes in the gradients of the amplitudes are virtually identical when $T_{\text{spin}} \gtrsim 6$ hours in all cases. This supports the statement made above about the coupling between the spin and orbital frequency having a significant effect on the difference in the SMA, $a_{\text{Plate}} - a_{\text{NoSRP}}$, when $T_{\text{spin}} \gtrsim 6$ hours (or $1/4T_{\text{orbit}}$), for all orientations considered in this study.

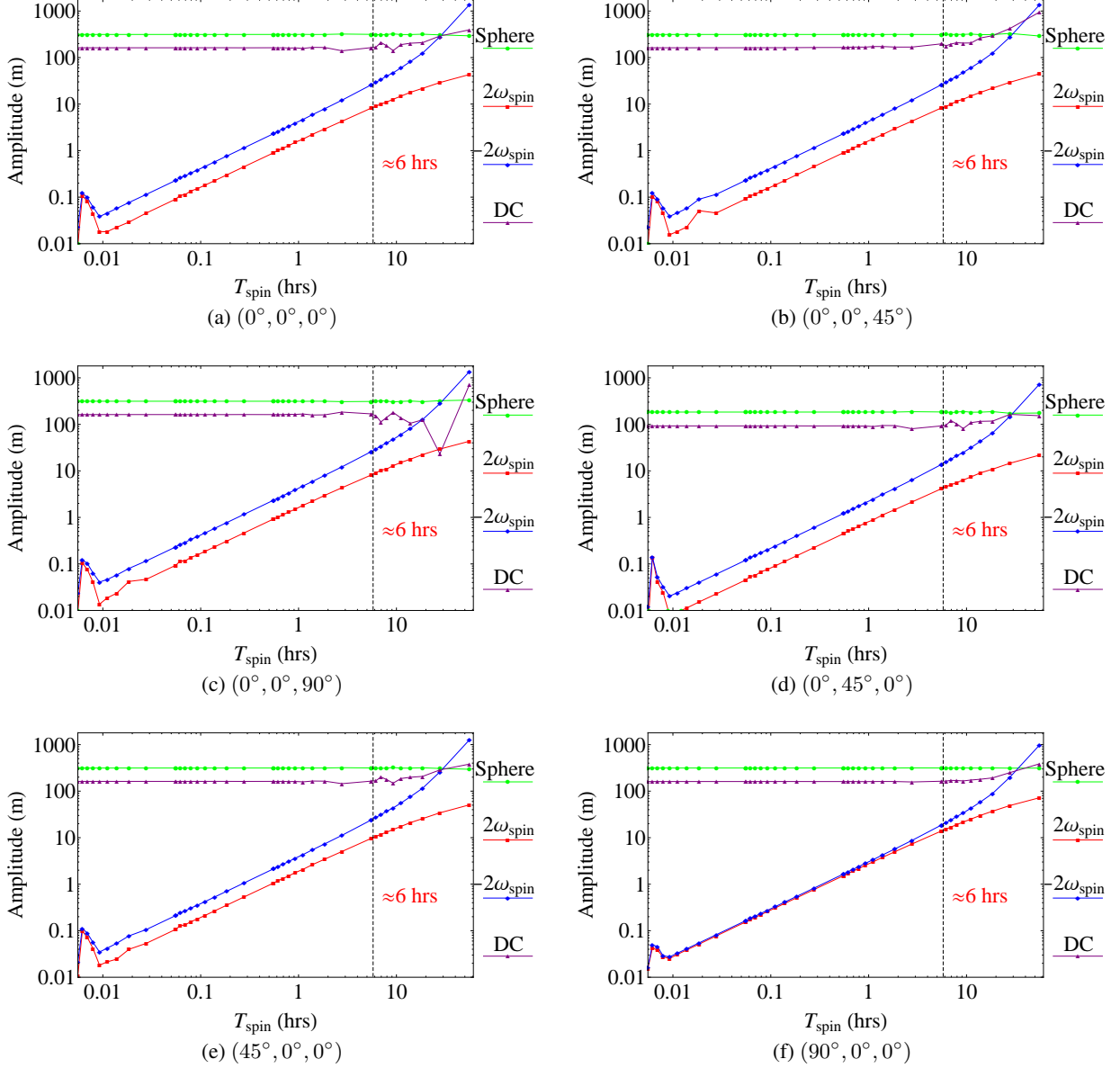


Fig. 5. Amplitudes and DC offset of the difference between the SMA of the spinning plate and SMA in the absence of SRP, $a_{\text{plate}} - a_{\text{NoSRP}}$, as a function of the spin period T_{spin} . In reference to Eq. (8), the amplitudes correspond to the spherical case when $n = 0$ (Green), $n = 2$ (Red), $n = -2$ (Blue), and absolute values of the DC offsets (Purple). The orientations are indicated in the sub-captions of each sub-figure.

3.4. Maximum Separation in the Radial and Along-Track Directions

Finally, we investigate the behavior of the maximum separation over the 10 day prediction span in the radial and along-track directions as a function of the spin period, T_{spin} . Fig. 6(a) provides these results for the initial orientation $(0^\circ, 0^\circ, 0^\circ)$, where we see once more that the maximum separation in the along-track direction [$\max(\Delta r_{\text{along}})$] (red curve) dominates that in the radial direction [$\max(\Delta r_{\text{radial}})$] (blue curve). By looking at the data for $\max(\Delta r_{\text{along}})$ in Fig. 6(a), the maximum along-track separation is almost independent of the spin period, T_{spin} , when it is small. However, observing the corresponding fit to $\max(\Delta r_{\text{along}})$ data (solid red curve), it is clear that the maximum along-track separation grows as T_{spin} increases and reaches the 1km threshold at $T_{\text{spin}} \approx 6.7$ hours; the maximum separation $\max(\Delta r_{\text{along}})$ then grows rapidly from that point onwards.

We now focus on Fig. 6(b) which gives $\max(\Delta r_{\text{radial}})$ and $\max(\Delta r_{\text{along}})$ for the initial rotation of 45° about the

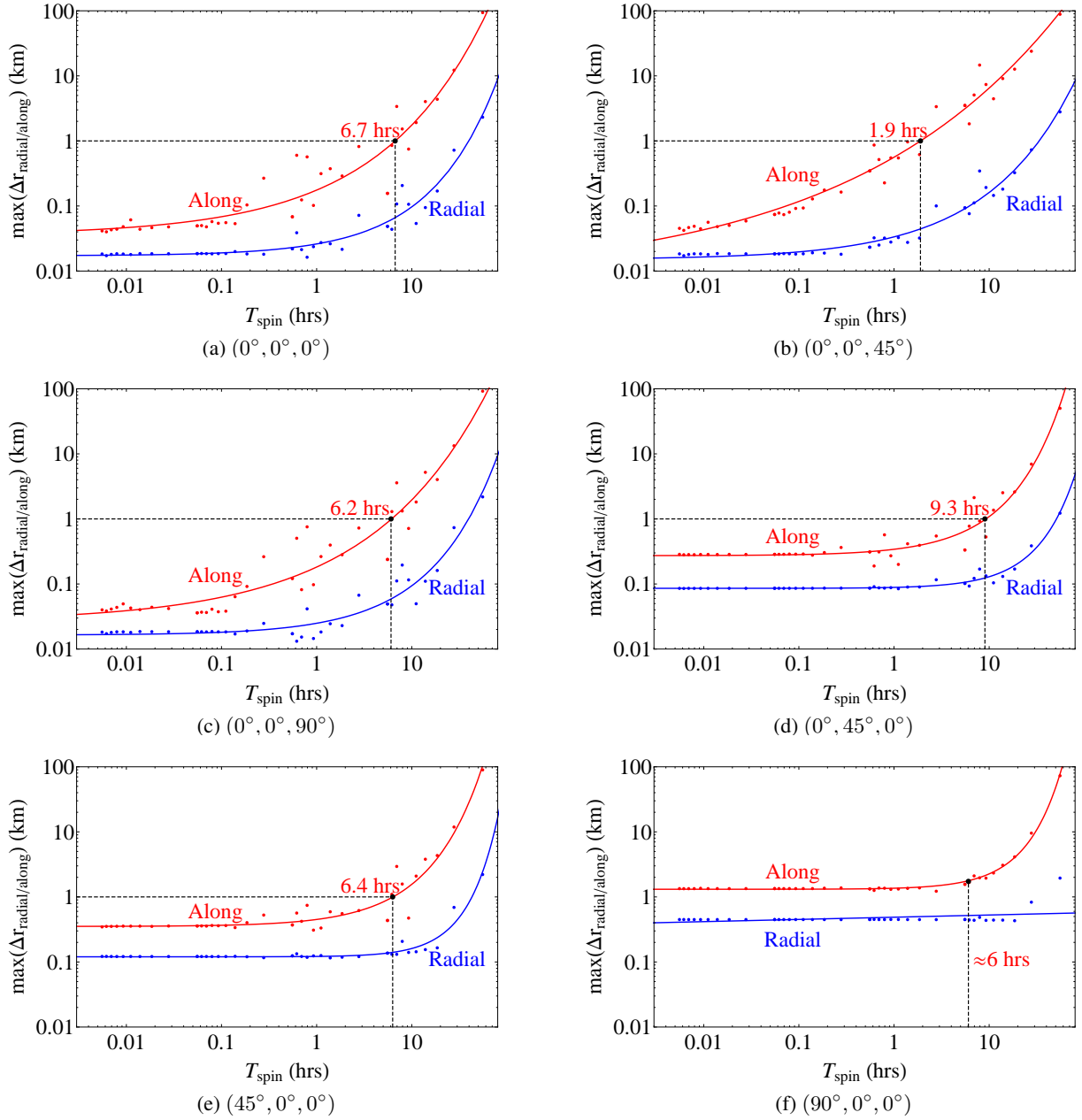


Fig. 6. Maximum separation over the 10 day prediction span in the radial (Blue) and along-track (Red) directions. The solid curves are corresponding fits to the data. The orientations are indicated in the sub-captions of each sub-figure.

z -axis. Interestingly, the maximum separation, $\max(\Delta r_{\text{along}})$, reaches 1km much sooner at $T_{\text{spin}} \approx 1.9$ hours, which is less than a third of that for the initial orientation $(0^\circ, 0^\circ, 0^\circ)$. This is expected since an orientation of $(0^\circ, 0^\circ, 45^\circ)$ yields a resultant force at $t = 0$ in both the radial and along-track directions due to specular and diffuse reflections. While this resultant force is averaged out when the plate spins quickly, it can not be captured effectively by the spherical SRP model as the spin rate slows down. This results in a larger separation in this case, compared to the $(0^\circ, 0^\circ, 0^\circ)$ orientation, as T_{spin} increases beyond ≈ 30 minutes.

The results of Fig. 6(c), show that the maximum separation in both the radial and along-track directions is qualitatively similar to that for the $(0^\circ, 0^\circ, 0^\circ)$ rotation. Furthermore, setting the initial orientation to $(0^\circ, 45^\circ, 0^\circ)$, it is found that the maximum separation, $\max(\Delta r_{\text{along}})$, is virtually constant at $\approx 300\text{m}$ until $T_{\text{spin}} \approx 1$ hour. This separation $\max(\Delta r_{\text{along}})$ reaches 1km at about $T_{\text{spin}} = 9.3$ hours and then increases rapidly thereafter. Speculatively, this higher

value for T_{spin} may be attributed to the plate never being fully exposed during a complete rotation for this orientation.

Comparing Figs. 6(e) and 6(f) shows that as θ_x increases, the maximum separation $\max(\Delta r_{\text{along}})$ becomes larger, but remains constant for longer for increasing T_{spin} . In addition, the separation $\max(\Delta r_{\text{along}})$ once again exhibits abrupt growth for $T_{\text{spin}} \gtrsim 6$ hours. Significantly, when $\theta_x = 90^\circ$ the maximum separation $\max(\Delta r_{\text{along}}) > 1\text{km}$ and remains constant for $T_{\text{spin}} \lesssim 6$ hours. This is consistent with the argument discussed in Sec. 3.2 describing Fig. 3, which highlights a resultant force that can not be averaged out as the plate spins or captured by the spherical SRP model.

To summarize, we see that when the coupling effects observed in Sec. 3.3 becomes significant, i.e., when $T_{\text{spin}} \gtrsim 6$ hours, the maximum separation $\max(\Delta r_{\text{radial/along}})$ undergoes rapid growth, irrespective of the orientation. Conversely, when the spin period $T_{\text{spin}} \lesssim 6$ hours, the maximum separation $\max(\Delta r_{\text{radial/along}})$ is highly dependent on the orientation.

3.5. Practical Implications

To finish with a practical context, say we were able to approximate the orientation, spin rate and area-to-mass ratio of a reasonably flat plate in a near-GEO orbit using a light curve analysis and/or a method like that proposed in [10]. Then results like that provided in Fig. 6 can be used to make an informed decision as to whether the spherical SRP model is sufficient or if a higher fidelity SRP model should be used. For example, suppose a flat plate with similar properties to the MSG-2 cooler cover was found to have a spin period of ≈ 6 hours. If at first the orientation was estimated such that the rotation axis coincided with the z -axis of the inertial system, then the worst case scenario would correspond to the $(0^\circ, 0^\circ, 45^\circ)$ orientation; see Fig. 6(b). In this case, the maximum separation in the along-track direction would be above 5km, which is larger than our 1km threshold. Based on this result, a decision would be made to use a non-spherical model for future predictions. Conversely, say the rotation axis was closer to being rotated by 45° about the y -axis, then in accordance with the results of Fig. 6(d), the maximum separation would be below the 1km limit safety zone. This would thus result in a decision to perform subsequent predictions using the spherical SRP model.

4. CONCLUSIONS

In this study, we began by deriving an expression to calculate the equivalent γ_{eqv} needed for simulations using the spherical SRP model. The results of those simulations, as well as those for the spinning plate, were compared by calculating the separation in the position in both cases. Interestingly, it was found that even when the plate spins quickly, the magnitude and behavior of the separation can change significantly for varying orientations. Nevertheless, most orientations considered for the object of interest used in this analysis, yielded a separation small enough such that the spherical assumption still provides reasonable predictions for the shortest spin period of $T_{\text{spin}} = 20$ seconds; for this spin period there was only one case which resulted in a separation which went beyond the chosen threshold of 1km for the object of interest.

The semi-major axis was then investigated to demonstrate the point at which the coupling between the orbital and spin frequency takes significant effect. It was shown that once the spin period approached approximately 6 hours, or 1/4 of the orbital period, the semi-major axis using the spinning plate model exhibited significant changes with respect to that of the spherical case. This was true for all orientations considered.

The maximum separation in the radial and along-track directions were then investigated as a function of the spin period. Excluding the case where the initial orientation was set to $(0, 45^\circ, 0)$, it was found that rotating about the z -axis initially by 45° yielded the shortest spin period at which the separation broke the 1km threshold. In contrast, the $(90^\circ, 0, 0)$ orientation resulted in the longest spin period. While the orientation had a dramatic effect on the behavior of the maximum separation when the spin period was small, when T_{spin} moved beyond approximately 6 hours the separation grew rapidly regardless of the orientation. Significantly, this region of rapid growth in the separation coincided with the regime where the coupling effects drove significant changes in the semi-major axis.

In the case of a plate in a near GEO orbit, this analysis provided insight into when a higher fidelity SRP model – based on a classical Lambertian BRDF approach – should be considered over the spherical assumption. This would be beneficial to members of the SSA community, of whom maintain their own catalogs or perform conjunction analyses.

ACKNOWLEDGEMENTS

The authors of this paper wish to acknowledge funding for this research project from the Cooperative Research Centre for Space Environment Management (SERC Limited) through the Australian Government Department of Industry, Innovation and Science. They would also like to take this opportunity to thank Dr. Sven Flegel, Dr. Steve Gower and Dr. Ben Greene of SERC for their insightful comments and feedback.

REFERENCES

- [1] D. A. Vallado. *Fundamentals of Astronautics and Applications*. Microcosm Press & Springer, CA & New York, 4th edition, 2013.
- [2] C. Früh and Schildknecht T. Investigation of properties and characteristics of high-area-to-mass- ratio objects based on examples of optical observation data of space debris objects in GEO-like orbits. Wailea, Maui, Hawaii, September 14-17 2010. Proceedings of the Advanced Maui Optical and Space Surveillance Technologies Conference.
- [3] M. D. Hejduk and R. W. Ghrist. Solar radiation pressure binning for the geosynchronous orbit. Girdwood, AK; United States, 31 July - 3 August 2011. 2011 AIAA/AAS Astrodynamics Specialist Conference.
- [4] D. M. Lucchesi. Reassessment of the error modelling of non-gravitational perturbations on LAGEOS II and their impact in the lensethirring determination. Part I. *Planetary and Space Science*, 49:447–463, 2001.
- [5] D. M. Lucchesi. The lageos satellites orbital residuals determination and the way to extract gravitational and non-gravitational unmodeled perturbing effects. *Advances in Space Research*, 39:1559–1575, 2007.
- [6] Y. R. Kim, S. Y. Park, E. S. Park, and H. C. Lim. Preliminary products of precise orbit determination using satellite laser ranging observations for ILRS AAC. *Journal of Astronomy and Space Sciences*, 29(3):275–285, 2012.
- [7] G. Zhao, Y. Zhao, M. Sun, and H Yu. H. Assessment of SLR observation performance using LAGEOS data. page 204, Poznań, Poland, October 13-17 2008. Proceedings of the 16th International Workshop on Laser Ranging.
- [8] J. W. McMahon and D. J. Scheeres. Improving space object catalog maintenance through advances in solar radiation pressure modeling. *Journal of Guidance, Control, and Dynamics*, 38(8):1366–1381, 2015.
- [9] T. Kelecy and J. Moriba. Analysis of orbital prediction accuracy improvements using high fidelity physical solar radiation pressure models for tracking high area-to-mass ratio objects. Darmstadt, Germany, 30 March - 2 April 2009. Proceedings of the Fifth European Conference on Space Debris.
- [10] T. Kelecy and M. Jah. Analysis of high area-to-mass ratio (HAMR) GEO space object orbit determination and prediction performance: Initial strategies to recover and predict HAMR GEO trajectories with no apriori information. *Acta Astronautica*, 69:551–558, 2011.
- [11] T. S. Kelso and S. Alfano. Satellite Orbital Conjunction Reports Assessing Threatening Encounters in Space (SOCRATES). <http://www.celestrak.com/SOCRATES/>.
- [12] S. K. Flegel, J. Gelhaus, M. Möckel, V. Braun, C. Kebschull, C. Wiedemann, P. Vörsmann, H. Krag, and H Klinkrad. Estimating the error in statistical HAMR object populations resulting from simplified radiation pressure modeling. Wailea, Maui, Hawaii, September 11-14 2012. Proceedings of the Advanced Maui Optical and Space Surveillance Technologies Conference.
- [13] D. J. Scheeres, A. J. Rosengren, and J. W. McMahon. The dynamics of high area-to-mass ratio objects in earth orbit: The effect of solar radiation pressure. *Advances in the Astronautical Sciences*, 140:1115–1138, 2011.
- [14] C. R. McInnes. *Solar Sailing: Technology, Dynamics and Mission Applications*. Springer-Praxis, 1 edition, 1999.
- [15] R. Burns, M. J. Gaborm, C. A. McLaughlin, K. K. Luu, and C. Sabol. Solar radiation effects on formation flying of satellites with different area to mass ratios. page 4132, Denver, CO, August 2000. AIAA/AAS Astrodynamics Specialist Conference.